ACCEPTED MANUSCRIPT

Li-doping effects on the native defects and luminescence of Zn_2GeO_4 microstructures: Negative thermal quenching

Jaime Dolado[a,b,*], Beatríz Rodríguez[a], Ruth Martínez-Casado[a], Igor Píš[c], Elena Magnano[c,d], Pedro Hidalgo[a] and Bianchi Méndez[a]

[a]*University Complutense of Madrid, Department of Materials Physics, Madrid, 28040, , Spain*

[b]*European Synchrotron Radiation Facility, 71 Av. des Martyrs, Grenoble, 38043, , France*

[c]*IOM-CNR, Istituto Officina dei Materiali, AREA Science Park Basovizza, Trieste, 34149, , Italy*

[d]*Department of Physics, University of Johannesburg, PO Box 524, Auckland Park, Johannesburg, 2006, , South Africa*

ABSTRACT

Novel transparent semiconducting oxides, such as Zn_2GeO_4, have emerged as key materials for a variety of optoelectronic applications due to their ultra-wide band gap. Owing to the critical role of native defects and impurities in the optoelectronical properties, investigation in detail of the electronic structure of these oxides has become a challenge, being luminescence technique a powerful way to gain insight into the electronic levels. Here, the luminescence temperature dependence of Li doped Zn_2GeO_4 microrods is analysed and discussed in the framework of the electronic levels structure related to native defects and Li impurities. Unlike the undoped material, the blue emission (2.8 eV) of Li-doped germanate exhibits a negative thermal quenching as its photoluminescence intensity increases with increasing temperature. The mechanisms underlying this anomalous behaviour are discussed with the aid of X-ray photoemission spectroscopy and first principles calculations. This study has helped us to understand the role of Li in the electronic structure and in the luminescence properties of Zn_2GeO_4. Our results highlight the versatility of Zn_2GeO_4 luminescence due to defect engineering through Li doping, which could be exploited in optoelectronic devices.

1. Introduction

Wide band gap (WBG) oxides (E_g > 3.5 eV) are versatile semiconductors with interest in a wide range of applications, from optoelectronic devices[1] or non volatile memories[2] up to energy related devices as fuel cells and batteries [3]. The physical properties of WBG oxides are strongly linked to their intrinsic defects and impurities, being oxygen vacancies the main responsible for the n-type conductivity[4] in most of them as well as for the luminescence in the visible range thanks to the electronic levels introduced in the band gap[5]. Among the WBG oxides, the interest in germanate oxides is recently pushing up since they can offer multi-functionality due to their crystalline and electronic structure[6]. In particular, Zn_2GeO_4 (ZGO) has emerged as a member of the ultra-WBG that allows ultraviolet light detection and absorption thanks to its band gap of 4.5 eV. Some works have reported the higher performance of solar blind-photodetectors or photocatalysis processes in systems based on ZGO[7, 8]. In addition, pure ZGO exhibits an intense white-bluish luminescence originated from native defects. Liu *et al.* suggested a first model to explain this emission in terms of the donor-acceptor pair (DAP) recombination, with the oxygen vacancies (V_O) and zinc interstitials (Zn_i) acting as donors and the Ge and Zn vacancies (V_{Ge} and V_{Zn}) acting as acceptors[9]. The potential of ZGO as phosphor material has also been reported in nanocrystals and in Mn-doped ZGO nanorods[10, 11]. Another field of interest in which ZGO oxide may offer solutions is in batteries as a promising electrode material that could replace pure Ge anodes and reduce the costs[12]. To all of these purposes, an in-depth study of the electronic states related to native defects in ZGO is of the utmost importance.

Recently, light alkaline cations, with obvious applications in energy storage devices and photo-catalysis, are gaining more and more interest as dopants in WBG oxides. Due to its small size and electronic configuration, Li doping offers versatility in terms of its influence on the electrical and optical properties, which is still under debate. For example, Li ion substitution for Zn (Li_{Zn}) in ZnO transforms it from n-type to p-type semiconductor by creating deep acceptor

*Jaime Dolado
✉ doladofe@esrf.fr (J. Dolado)
ORCID(s):

levels, whereas Li occupying an interstitial position (Li$_i$), behaves as an electron donor[13]. On the other hand, lithium related deep and shallow levels in ZnO have also been claimed as responsible for the yellow emission band [14]. In addition, some recent works have reported the influence of Li impurities on the morphology of Ga$_2$O$_3$ microrods[15] and in ZnO nanostructures[16], which has been attributed to some alteration of their surface energy properties. To the best of our knowledge, there is no previous work on ZGO:Li material.

In this work, Li doped ZGO microstructures have been produced by a thermal evaporation method, through the vapor-solid mechanism, of a mixture of Li$_2$CO$_3$, ZnO and Ge precursors. The effective incorporation of Li, which is often difficult to assess, has been confirmed by synchrotron radiation X-ray photoelectron spectroscoy (XPS) measurements. The XPS results also suggest that the native defects landscape has been affected by the Li doping, inducing changes in the luminescence properties of ZGO. Precisely, the temperature dependence of the photoluminescence (PL) in undoped and Li doped ZGO shows different trends. Particularly, a negative thermal quenching (NQT) and persistent bluish emission is achieved in Li-doped material. The PL results have been discussed in the framework of the electronic energy levels structure related to native defects, and then compared with first-principle calculations of electronic states in ZGO containing V$_{Zn}$, Li$_i$ and Li$_{Zn}$ point defects. Finally, based on our both theoretical and experimental results, a more complete picture of the luminescence mechanisms in ZGO is proposed.

2. Experimental methods

Synthesis

The synthesis of the ZGO microstructures were carried out by a thermal evaporation method. The material precursor of undoped ZGO was a compacted mixture of ZnO:Ge powders (1:1 wt %) whereas Li$_2$CO$_3$ powders were added in proportions of 5, 10, and 15 wt % related to the total ZnO:Ge amount, for the Li doped material. The chemicals used were ZnO (Sigma Aldrich, 99.9% purity), Ge (Goodfellow, 99.999% purity) and Li$_2$CO$_3$ (Analytical Grade ACS) powders. The compacted pellets, which acts as source and substrate without the need of an extra catalyst, were placed on an alumina boat and annealed under an Ar flow of 1.5 l/min in a tubular furnace at 800 ºC for 8 h. As a result, the pellet appeared covered by a white mat of microstructures that were gently deposited on suitable substrates for their further characterization. Li-doped samples were labeled as ZGO-Lix, where x is the percent of Li$_2$CO$_3$ powders added to the precursor mixture.

Characterization techniques

The structural characterization was assessed by X-ray diffraction (XRD) and Raman spectroscopy techniques. XRD patterns were recorded using a a PANalytical Empyrean diffractometer (X-ray of the Cu lines $K_{\alpha_1} + K_{\alpha_2}$). Diffractograms were collected working at 45 kV and 40 mA using Bragg-Brentano geometry, for values between $10º \leq 2\theta \leq 60º$, with step size of 0.010º and 3 s per step. Raman measurements have been carried out on a Horiba Jobin Yvon LabRam HR800 system with a CCD detector, coupled to an Olympus BXFM-ILHS confocal microscope and equipped with a 325 nm wavelength He-Cd laser.

The morphology characterization has been performed in a FEI Inspect scanning electron microscope (SEM). Energy dispersive spectroscopy (EDS) measurements have been carried out with a Bruker AXS XFlash 4010 detector installed in a Leica 440 Stereoscan SEM.

The XPS measurements were carried out at the BACH beamline of CNR at the Elettra synchrotron (Trieste, Italy). XPS spectra were acquired with a hemispherical electron energy analyzer (Scienta R3000, VG Scienta) at photon energies of 110 and 650 eV at a total instrumental resolution of 0.2 eV. Binding energies of XPS spectra were calibrated using the C 1s position (assuming that C 1s is at 284.8 eV). Zn and Ge oxidations states in Zn and Ge 3d spectra were fitted by single or multiple Gaussians functions in the ZGO and ZGO-Li10 samples, respectively.

PL measurements were performed on an Edinburgh Instruments FLS1000 system from 4 K to RT, excited with a 450 W ozone free xenon arc lamp and using a high-gain photomultiplier detector (Hamamatsu R928P), which covers the range from 185 nm – 900 nm. A liquid helium cryostat from Oxford Instruments (OptistatCF) is used to cool the sample. In addition, μ-PL images were collected in the confocal microscope used for Raman measurements.

Density functional theory simulations

The Density Functional Theory (DFT) calculations have been performed using the CRYSTAL program[17], in which the crystalline orbitals are expanded as a linear combination of atom-centered Gaussian orbitals, the basis set. The zinc, oxygen, germanium, and lithium ions are described using all-electron basis sets contracted as s(8) sp(64111)
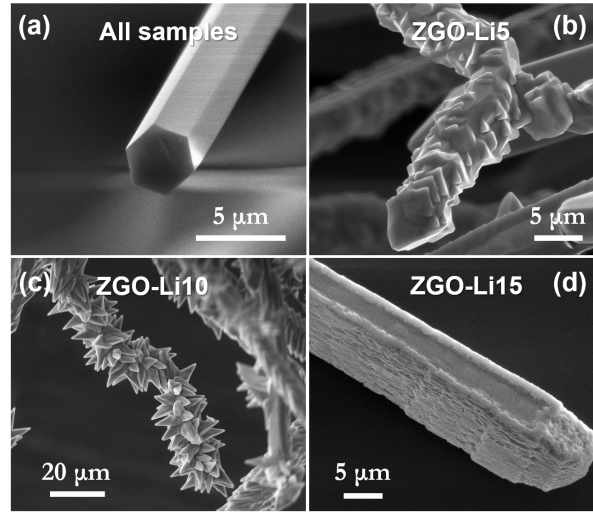
Fig. 1: SE images of (a) generic hexagonal-shaped microrod, (b) ZGO-Li5 distorted microstructure, (c) ZGO-Li10 microstructure with platelet-shaped branches and (d) ZGO-Li15 stratified microstructure.

d(41), s(8) sp(611) d(1), s(9) sp(76) d(511) sp(31), and s(511) p(1) respectively. Electronic exchange and correlation were approximated by using the Heyd-Scuseria-Ernzerhof (HSE) screened hybrid functional[18]. In particular, the HSE06 functional with a mixing parameter of 0.25 has been used to describe the fundamental band gap and electronic structure of ZnO, giving rise to a band gap of 4.62 eV, which is in excellent agreement with the experimental value and validates the considered model for ZGO[19]. Integration over the reciprocal space was carried out using Monkhorst-Pack meshes of $6 \times 6 \times 6$. The self-consistent field algorithm was set to converge at the point at which the change in energy was less than 10^{-7} Hartree per unit cell. The internal coordinates have been determined by minimization of the total energy within an iterative procedure based on the total energy gradient calculated with respect to the nuclear coordinates. Convergence was determined from the root-mean-square (rms) and the absolute value of the largest component of the forces. The thresholds for the maximum and the rms forces (the maximum and the rms atomic displacements) have been set to 0.00045 and 0.00030 (0.00180 and 0.0012) in atomic units. Geometry optimization was halted when all four conditions were satisfied simultaneously.

3. Results and discussion

Morphological, structural and chemical characterization

Undoped ZGO and Li doped ZGO-Li5, ZGO-Li10 and ZGO-Li15 samples were obtained following the above described procedure. Photographs of the four pellets after the thermal treatment are shown in Figure SI-1. It is interesting to note that the number of microstructures is high in undoped ZGO and ZGO-Li5, and decreases with increasing Li concentration in the precursor mixture. Figure 1 shows the morphology of the representative structures obtained in the different samples. In all of them, hexagonal-shaped microrods are formed as that shown in Figure 1a (see also Figure SI-2), being the only morphology observed in undoped ZGO. The microrods had cross-sectional dimensions in the range of 1 μm to about 10 μm and their lengths extend to hundreds of microns. However, in ZGO-Li samples additional morphologies are easily found. In the case of ZGO-Li5, some structures show a distorted surface due to the formation of small plates on it, as it is shown in Figure 1b. In ZGO-Li10, structures with triangular-shaped platelet branches (P-B) are formed (see Figure 1c). Finally, ZGO-Li15 samples show some stratified microrods, which seem to be formed by stacking of layers (see Figure 1d). These results show that Li addition in the synthesis route influences the growth process in the formation of the ZGO microstructures. Previous works have reported the formation of novel shapes in oxide micro- and nanostructures by the incorporation of impurities during vapor-solid synthesis processes, as crossing wires or hierarchical structures[20, 21]. In the case of Li-doped oxides, such as ZnO, SnO$_2$ or Ga$_2$O$_3$[16, 22, 15], these changes in morphology have been considered as a proof of the effective incorporation of Li into the oxide material.
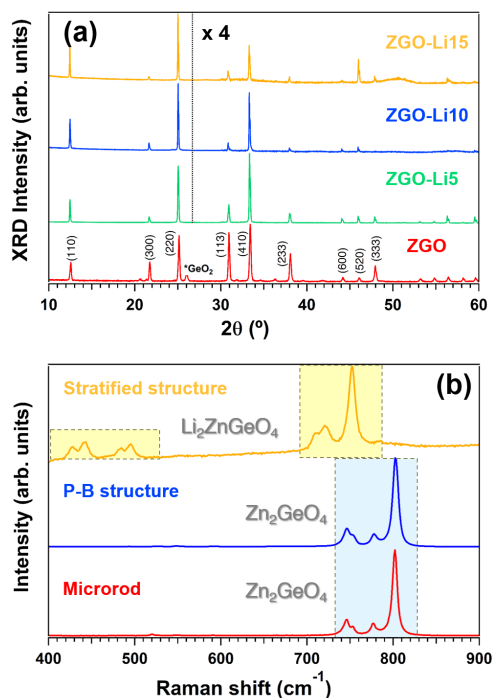
Fig. 2: (a) XRD pattern acquired from the undoped ZGO (red line), ZGO-Li5 (green line), ZGO-Li10 (blue line) and ZGO-Li15 (orange line) samples. (b) Raman spectra acquired on a generic microrod (red line), a P-B microstructures obtained in ZGO-Li10 (blue line) and a stratified structure obtained in ZGO-Li15 (orange line).

The crystal structure of the samples has been assessed by XRD and Raman measurements. Figure 2a shows the XRD diffractograms of both ZGO and the three ZGO-Li samples after the thermal treatment. All the peaks correspond to the rhombohedral crystal structure of ZGO (ICSD collection code: 68382). No extra peaks associated with other phases that may have formed during thermal treatment have been identified.

Since Li-containing precursors produce microstructures with different morphologies than hexagonal microrods, it would be of interest to individually study the crystalline structure of these structures. To this purpose, the representative structures were deposited on a piece of Si wafer to carry out micro-Raman measurements in the confocal microscope. The Raman spectrum of a generic microrod (red curve in Figure 2b) shows the characteristic Raman peaks of the rhombohedral structure of ZGO at 745, 751, 777 and 802 cm^{-1} associated with Ge-O-Zn symmetric and asymmetric vibration modes and the O-Ge-O bending and stretching modes[23]. Similar Raman spectra were obtained from the distorted structures of ZGO-Li5 (not shown) and from the P-B structures of ZGO-Li10 (blue curve in Figure 2b). However, the stratified structures of ZGO-Li15 shows a modified Raman spectrum (orange curve in Figure 2b) with peaks at 427, 440, 484, 495, 710, 720 and 752 cm^{-1}, suggesting that another compound might be formed. Precisely, these Raman peaks match with those reported for the Li_2ZnGeO_4 compound, with a lattice consisting of a distorted hexagonal array of GeO_4 tetrahedra, linked together by LiO_4 and ZnO_4 tetrahedra[24]. These Raman results are consistent with the quantitative composition analysis carried out by EDS in the stratified structures in which the Zn/Ge ratio is close to 1 (Table SI-1), as expected for Li_2ZnGeO_4. The formation of this compound in ZGO-Li15 would suggest that Li is preferentially occupying Zn sites in the ZGO lattice.

XPS results

Additional information about the influence of Li on the structural and chemical properties of ZGO was obtained by means of XPS measurements. For this purpose, ZGO and ZGO-Li10 microstructures were placed on an indium substrate, in order to reduce charging effects while measuring. The ZGO-Li10 sample has been chosen because it still retains the ZGO phase contrary to the ZGO-Li15 one. Figures 3a and b show the high-resolution XPS spectra of Li 1s core level (55 eV) for undoped ZGO and ZGO-Li10 samples respectively. In order to increase the photoemission cross-section, a photon energy of 110 eV was used. The results confirm the Li incorporation in the ZGO-Li10 samples.

ZGO   **ZGO-Li10**
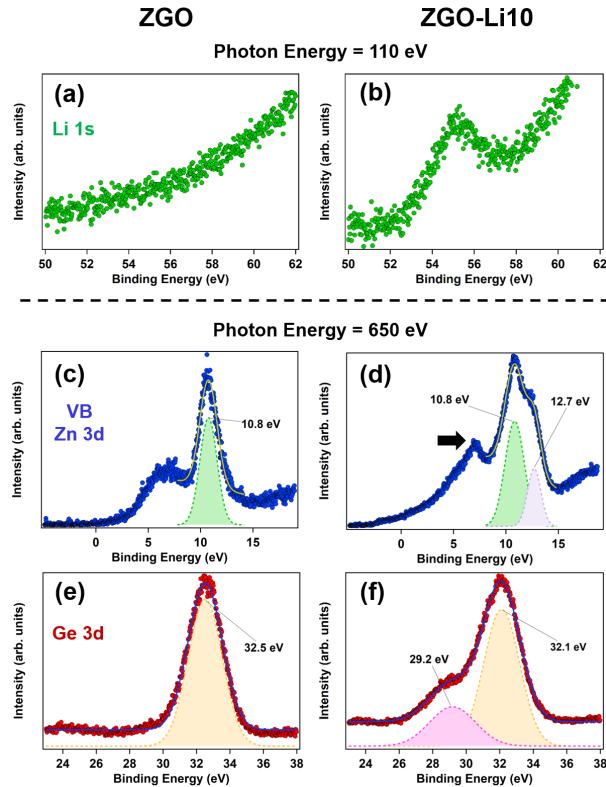
Fig. 3: Li 1s core level XPS spectra of (a) ZGO and (b) ZGO-Li10 taken with a photon energy of 110 eV. (c) & (d) VB-Zn 3d and (e) & (f) Ge 3d core level XPS spectra of ZGO and ZGO-Li10 samples taken with a photon energy of 650 eV.

The presence of Li cations as interstitials inside the hexagonal rings of the ZGO structure or as substitutional impurities may have an impact on the core levels of the matrix elements and in the valence band (VB). Figures 3c-f show the VB and core level XPS spectra of Zn 3d and Ge 3d acquired with a photon energy of 650 eV from undoped ZGO and ZGO-Li10 samples. The Zn 3d line is peaked at 10.8 eV in both samples (the component at 12.7 eV in ZGO-Li10 comes from the In 4d level), in good agreement with the literature[25]. However, a notable result regards the VB. The top of the VB of ZGO-Li10 appears at binding energy significantly higher (about 0.3 eV) than the undoped ZGO. According to the chemical bonds in ZGO, the VB is composed of O 2p, Zn 3d orbitals and hybridized Ge 4s4p orbitals[26]. Thus, the line-shape of O 2p related-orbitals in the top of the VB is modified in Li-doped samples (marked with an arrow in Figure 3d), which could be related to the presence of a higher concentration of oxygen vacancies in ZGO-Li.

Regarding Ge 3d core level, Ge oxidation states were fitted to a single component at 32.5 eV in undoped structures, linked to the O-Ge-O bonds in GeO_4 tetrahedral[27]. For the ZGO-Li10 sample, an extra component appears at 29.2 eV related to the neutral Ge, which could be related to some distortion of the GeO_4 tetrahedral in the lattice. This lattice distortion could lead to an anomalous Ge 3d core level, as it has been reported in other alloys[28]. In addition, the presence of Ge in a lower oxidation state supports as well the presence of oxygen vacancies in terms of the charge balance in the crystal.

These findings demonstrate that Li incorporation in ZGO has an impact on its native defects landscape. As a consequence, the electronic states structure might also be altered in ZGO-Li in comparison with undoped ZGO. A rather easy way to probe defect-related electronic states is by luminescence techniques since they do not require of electrical contacts. The results of this study are presented in the next section.

Photoluminescence study. Negative thermal quenching

PL measurements of both undoped and Li-doped ZGO microstructures generously deposited on a silicon wafer have been conducted as a function of temperature. As the aim of this work is to show the effect of Li doping on the
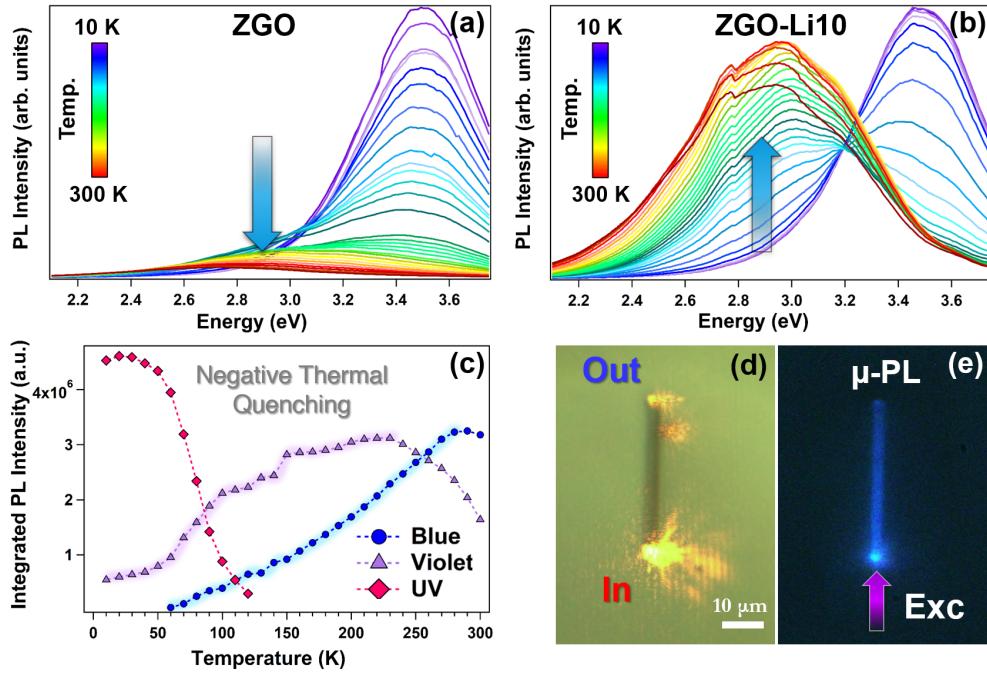
Fig. 4: PL spectra as a function of the temperature obtained under 4.86 eV excitation energy of (a) undoped ZGO and (b) ZGO-Li10 samples. (c) Variation of the integrated PL intensity as a function of temperature for the different bands observed in ZGO-Li10 sample (blue, violet and UV). The glowing areas indicate the temperature ranges in which the NQT occurs. (d) Optical image of a ZGO-Li10 microrod showing the waveguiding behavior of the structure. (e) μ-PL image of the same microrod in dark field showing persistent luminescence.

optical properties of ZGO, the ZGO-Li10 was selected as representative Li-doped sample. Figures 4a and 4b show the PL spectra from 10 K to 300 K acquired on the undoped and the ZGO-Li10 samples, respectively, excited with 4.86 eV. This energy was intentionally selected in order to achieve above band gap excitation conditions and eventually observe all possible radiative recombination paths. The main emission in both samples at 10 K is an intense UV band, with a main component at 3.5 eV, attributed to recombination between V_O donors and VB[19]. As the temperature increases, a blue-violet band with two components, 2.8 (blue) and 3.1 eV (violet), arises from the activation of DAP transitions, which could involve cation vacancies (V_{Ge} or V_{Zn}) as acceptor centres[9].

The intensity of defect-related PL in semiconductors generally changes with temperature, and it usually decreases exponentially above some critical temperatures in a process called PL positive thermal quenching (PTQ) due to the increase in the nonradiative rate[29, 30]. This PL quenching is observed in the temperature PL evolution of the undoped sample, Figure 4a, as an overall decrease of PL emission. However, the PL spectrum from the ZGO-Li10 sample behaves in a different way, as Figure 4b shows. The PTQ of the UV band is accompanied by an increase of the intensity of the blue-violet band as the temperature scales up, becoming the main emission at room temperature (RT). This anomalous behaviour in which the PL intensity rises with increasing temperature has been observed for different semiconductors and is often called NTQ[29, 31, 32, 33].

In order to examine the PL temperature dependence in more detail, the deconvolution to Gaussians of the PL emission at each temperature was carried out (see Figure SI-3). Figure 4c shows the integrated PL intensity of each band versus temperature. It can be clearly seen that from 50 K onward the intensity of the UV band starts to decrease exponentially with increasing temperature. In contrast, the violet and the blue bands rise in intensity with increasing temperature. In particular, the intensity of the blue band maximum occurs close to RT.

The NTQ behaviour has been explained in different ways, depending on the centres involved in the luminescence band[30]. In the case of the PTQ of an intense band in favor of a rise of other bands, the reason would be the competitiveness between the recombination paths for the photogenerated carriers, as occurs in GaN and ZnO[34]. Alternatively, the NTQ has also been attributed to the presence of intermediate states below the initial state of PL transitions, which are activated at certain temperature. For example, this mechanism has been claimed to explain the

Table 1
Activation energies for the thermal quenching processes of the PL emission of ZGO-Li10 microrods according to the equation 1.

Band	E_1' (meV)	E_1 (meV)	E_2 (meV)	Quenching type
UV	-	46	-	PTQ
Violet	21	17	158	NTQ & PTQ
Blue	33	-	-	NTQ

NTQ of the green emission in BiFeO$_3$ nanowires in terms of the electrons de-trapping from surface defect states below the conduction band at higher temperatures[35].

The multi-level model developed by Shibata[36] has been often used to describe the PL temperature dependence, including both PTQ and NTQ, by means of the following expression:

$$I^{PL}(T) = I_0^{PL} \frac{1 + \sum_{q=1}^{n} C_j \exp\left(-E_q'/k_B T\right)}{1 + \sum_{j=1}^{m} D_j \exp\left(-E_j/k_B T\right)} \tag{1}$$

where I_0^{PL} denotes the PL emission intensity in the limit of low temperatures, k_B is Boltzmann's constant, n is total number of intermediate states with respective activation energy E_q', and m is the total number of nonradiative recombination processes, each having an activation energy E_j. D_q and C_j are coefficients for the intermediate and nonradiative processes, respectively. In this formula, the exponential term in the denominator is related to the PTQ process, while the exponential term in the numerator is used to describe the NTQ process. The experimental data shown in Figure 4c have been fitted to Eq.1 considering a single intermediate state ($n = 1$) and up to two possible nonradiative channels ($m = 2$), in accordance with the observed behaviour of PL intensity of ZGO-Li10 (see Figure SI-4). The obtained activation energies for the different bands are summarized in Table 1.

The fitting curves match well to the experimental data, indicating that the model is suited to represent the variation of PL intensity with temperature. The UV band only exhibits PTQ, extinguishing completely for temperatures above 120 K. Moreover, the activation energy obtained is significantly different from that obtained for the undoped ZGO[37], suggesting that it is possible that Li doping changes the ratio between the radiative mechanism that gives rise to the UV band and the nonradiative mechanism that reduces its intensity. In the case of the violet band, there is a first temperature interval in which the intensity increases and a second one in which it decreases. Therefore, it is necessary to include activation energies of both processes (PTQ and NTQ) to achieve a proper fitting of the experimental data over the whole temperature range. Finally, the blue band exhibits a pure NTQ over the whole temperature range, reaching its maximum at RT.

The enhancement of the blue emission is evident when assessed with the aid of a UV laser (3.82 eV) at RT. Figure 4d shows an optical image of one microrod of ZGO-Li10 exhibiting two bright spots at the ends as a result of the light propagating across the microrod when the laser strikes one end of the rod. In addition, Figure 4e shows the corresponding μ-PL image of the same microrod, in which a persistent bluish luminescence, originated as the laser goes through the rod, is achieved. The persistent luminescence is much more prominent in the Li-doped structures than in the undoped microrods (see Figure SI-5). A long-lasting photoluminescence has been observed previously in ZGO by Takahashi and co-workers[38] and attributed to the role of Zn$_i$-related levels that acted as electron traps. Therefore, Li$_i$ defects could be performing the same role in these ZGO-Li10 microrods, as in the case of Mg-doped ZGO microrods[39].

The origin of the blue band in undoped ZGO is uncertain and often is attributed to DAP transitions[40], in which V$_{Zn}$ could play a key role in this issue. This defect would act as a nonradiative centre through the recombination of the electrons of this level with the holes of the VB. At the same time, it could act as a radiative deep acceptor centre, through the recombination of electrons from the V$_O$ level with the holes of this level. At low temperature, this centre would be saturated with electrons, resulting in no free holes and the electrons in the V$_O$ level would recombine with the VB holes, leading to the only UV emission. As the temperature increases, the acceptor levels can thermally emit

holes towards the VB. This would cause the deep acceptor levels to have more holes with which to recombine their electrons, thus increasing both nonradiative recombinations (electrons from the V_{Zn} levels with holes in the VB) and blue emission (electrons from the V_O level with holes in the V_{Zn}). This would explain the PTQ of the UV band in the ZGO microrods, which left the blue emission as the only one to RT[37]. However, the NTQ behaviour of the blue emission in ZGO-Li remains obscure.

This change could have been promoted by the formation of complex defects involving V_{Zn} and Li ions in the lattice, in agreement with the charge transfer suggested by the above XPS results. Li could be incorporated by replacing Zn in the structure of the ZGO microrods in agreement with the fact that Li_2ZnGeO_4 phases had been detected in the Raman spectra from some structures in ZGO-Li15. However, Li_i defects cannot also be ruled out, as the persistent bluish PL suggests. In the next section, first principle calculations of the electronic band structure in defect-free and defective ZGO-Li are presented.

First-principles calculations
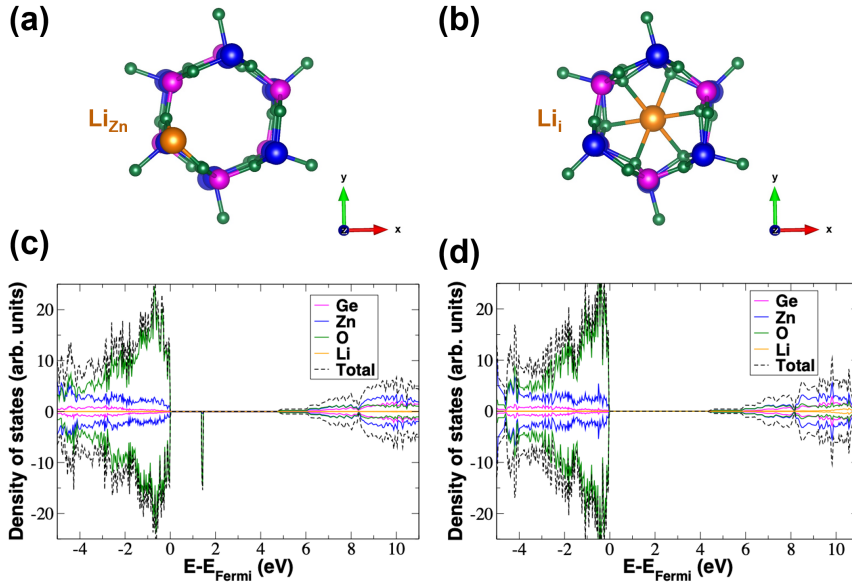
Fig. 5: ZGO unit cell with (a) a Zn atom replaced by Li and (b) a Li interstitial defect. Zn, Ge, O and Li atoms are represented as blue, magenta, green and orange circles, respectively. DOS of ZGO with (c) Li_{Zn} and (d) Li_i defects.

The above experimental results in ZGO-Li suggest that Li might be incorporated in ZGO replacing Zn and/or in an interstitial way. Besides, there could be an interplay between V_{Zn} and Li_{Zn} or Li_i defects, which lead to the observed NTQ of the blue emission and the additional features in the VB XPS spectra. Previous DFT calculations allowed us to discern that the blue emission of undoped ZGO is related to the radiative recombination of electrons from the V_O donor level to the V_{Zn} acceptor level, which introduces two electronic states in the band gap at 1.4 eV and 1.6 eV[19]. Now, the electronic structure and Density Of States (DOS) has been calculated for Li-related defects.

Figure 5 shows the optimized structure and the DOS of the Li-doped ZGO unit cell with Li_{Zn} and Li_i defects (see Figures 5a and b). For the Li_{Zn} case, the unpaired electron introduced by the substitution of one Zn atom with one Li atom leads to a DOS split into spin-up and spin-down states, and a dopant-induced state appears within the band gap at 1.4 eV above the top of the VB (Figure 5c). This state comes from the spin moment of 0.89 μ_B (the Bohr magneton) generated in one oxygen atom. On the other hand, the DOS simulated for Li_i (Figure 5d), shows no additional states within the band gap and no spin moment have been observed for this system. The Mulliken population (number of electrons) for the different atoms in both cases can be seen in Table SI-2.

It has to be noticed that both V_{Zn} and Li_{Zn} defects introduce states at 1.4 eV, which could indicate that the states coming from Li_{Zn} could also give rise to blue emission related to V_{Zn}. However, the formation of additional complex defects in ZGO-Li cannot be ruled out. As a next step, the complexes V_{Zn}-Li_{Zn} and V_{Zn}-Li_{Zn}-Li_i defects (see Figures 6a and b) have also been simulated by DFT calculations. The DOS in both cases reveals a decrease in

the band gap of 0.3 eV with respect to the perfect material (4.5 eV according to DFT calculations[19]). Besides, three electronic states appear at 1.4, 1.6 and 2 eV, coming from a spin moment of 0.88, 0.95 and 0.93 μ_B in three oxygen atoms, respectively, in the case of V_{Zn}-Li_{Zn} defects. On the other hand, two electronic states can be seen in the band gap at 1.6 and 2.1 eV as a result of the spin moment of 0.95 and 0.91 μ_B in two oxygen atoms, in the case of V_{Zn}-Li_{Zn}-Li_i defects. The Mulliken population for the different atoms in both cases can be seen in Table SI-2.

The formation energy (E_f) of the V_{Zn} in each case has also been calculated by DFT. The data show that the E_f decreases from 8.22 eV in material with no extrinsic defects up to 7.78 eV for V_{Zn}-Li_{Zn}, and decreases even further, up to 7.23 eV, for the V_{Zn}-Li_{Zn}-Li_i complex. This feature has been previously reported for other oxides, such as ZnO[41]. Also, Yi *et al.* have reported that, at sufficiently high concentration, Li_i and Li_{Zn} defects in ZnO form a stable defect complex which helps to lower the formation energy of V_{Zn}[42]. Both statements are in perfect agreement with the DFT results presented here. Li leads to the creation of both types of defects (Li_{Zn} and Li_i) in ZGO, which form a complex that assist the formation of V_{Zn} by lowering its formation energy. This increase in V_{Zn} concentration would favour the enhancement of the blue emission seen in the previous PL experiments. Furthermore, the presence of Li_i would support the persistent blue luminescence seen by μ-PL imaging, as these defects act as electron traps.
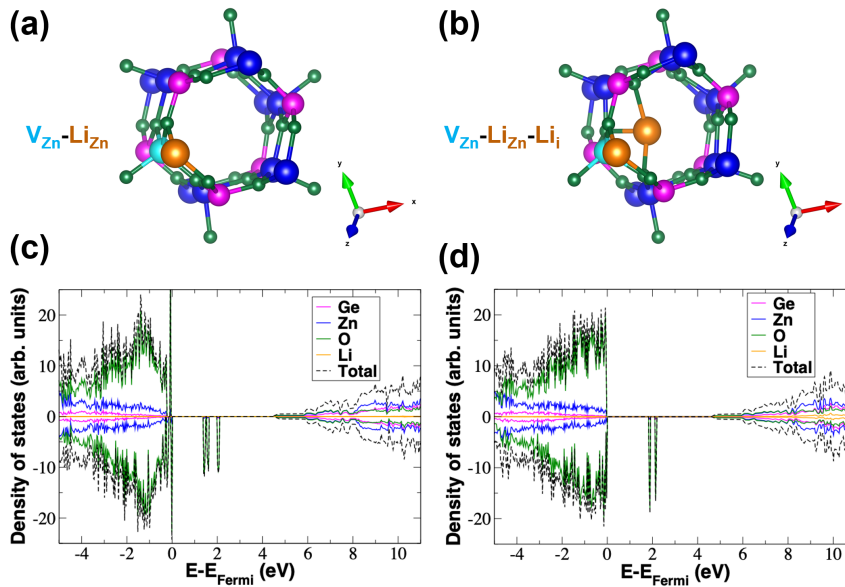
Fig. 6: Optimized structure of ZGO with (a) V_{Zn}-Li_{Zn} and (b) V_{Zn}-Li_{Zn}-Li_i defects. Zn, Ge, O, Li atoms and V_{Zn} are represented as blue, magenta, green, orange and cyan circles, respectively.. DOS of ZGO with (c) V_{Zn}-Li_{Zn} and (d) V_{Zn}-Li_{Zn}-Li_i defects.

Energy band model

Finally, based on all above results an energy band model that could explain the luminescence behaviour of the Li doped ZGO in terms of the defect-related electronic levels is proposed in Figure 7. The blue emission is related to DAP transitions between V_O (donors) and the electronic level created by the V_{Zn} and Li_{Zn} (acceptors). At low temperatures, these centres would be saturated with electrons, which blocks the DAP recombination and promotes the UV emission (electrons in the V_O level recombining with the holes ion the VB), as shown in Figure 7a. As the temperature increases, acceptor levels near the VB can thermally emit holes towards the VB, as Reshchikov suggests to explain the NTQ [34]. In addition, for every Li atom that is introduced into the lattice replacing Zn, a hole is added to the VB. The increase of holes in the VB means that the V_{Zn}-Li_{Zn} levels are no longer saturated and electrons can recombine from the V_O donor level to the V_{Zn}-Li_{Zn} acceptor levels, as shown in Figure 7b. Therefore, this model would explain the enhancement of the blue emission at RT (NTQ behaviour) in Li-doped ZGO microrods due to the increase of electronic states that originate this emission by the formation of Li_{Zn}-Li_i defect complexes.
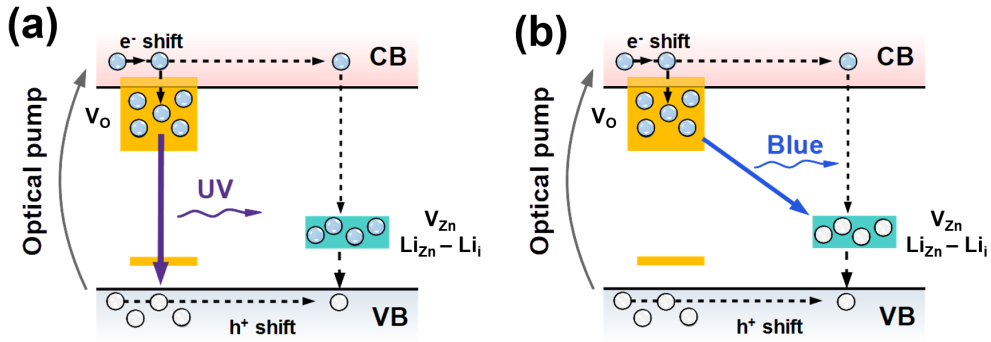
Fig. 7: Suggested energy band model to explain the NTQ behaviour of the blue band in ZGO-Li10 microstructures (a) in the low temperature range (4 - 50 K) where the blue band is not visible and (b) from 50 K onwards, when the UV band is quenched and the increase in intensity of the blue band begins. The solid lines represent radiative mechanisms, while the dashed lines represent nonradiative mechanisms.

4. Conclusions

In summary, an effective Li doping of ZGO microstructures has been achieved by a thermal evaporation method. Li_2CO_3 powders were added to a mixture of ZnO:Ge in several proportions (5, 10, and 15 wt % related to the total ZnO:Ge amount). In samples grown with 5 and 10 wt % of Li_2CO_3, the structural study has revealed the incorporation of Li as a dopant, while Li_2ZnGeO_4 structures were also formed in the sample grown with 15 wt % of Li_2CO_3. XPS measurements show that Li doping has an impact on native defects landscape and valence band supporting the formation of new native defects involving Li ions. The temperature dependence study of the PL also reveals a different behaviour between undoped and Li-doped samples. Both samples show an intense UV emission at low temperature, and a blue-violet emission coming from DAP transitions emerges as temperature raises. However, this emission undergoes a negative thermal quenching in ZGO-Li, which is not present in undoped ZGO. The results have been explained in the framework of the findings of first-principles calculations in ZGO containing several point defects, that mix V_{Zn} and Li ions. The DFT results have shown that Li has some major effects on the ZGO electronic structure: First, when Li enters the lattice in substitution of Zn, a new electronic state is generated at 1.4 eV, very close to the one produced by the V_{Zn} (defect related to the ZGO blue emission). Secondly, the calculations showed a decrease, with respect to the undoped sample, in the formation energy of the V_{Zn} when a Li_{Zn}-Li_i complex was formed. Finally, a decrease in the band gap with respect to the perfect material. These changes in the electronic structure revealed the significant role of Li in the NTQ process, which could be of great interest for the incorporation of ZGO in optoelectronic devices. Therefore, these results highlights the improvement of the optoelectronic properties of Li-doped ZGO microrods as potential candidates as visible light emitting diodes.

Conflicts of interest

There are no conflicts to declare.

Acknowledgements

CRediT authorship contribution statement

Jaime Dolado: Methodology, Investigation, Writing - original draft, Data curation, Visualization. **Beatríz Rodríguez:** Data curation, Visualization. **Ruth Martínez-Casado:** Methodology, Data curation, Visualization, Writing - review & editing. **Igor Píš:** Methodology, Writing - review & editing. **Elena Magnano:** Methodology, Writing - review & editing. **Pedro Hidalgo:** Conceptualization, Methodology, Writing - review & editing, Supervision. **Bianchi**

Méndez: Conceptualization, Methodology, Writing - original draft, Writing - review & editing, Supervision, Funding acquisition.

References

[1] X. Yu, T. J. Marks, A. Facchetti, Metal oxides for optoelectronic applications, Nature Materials 15 (2016) 383–396.

[2] A. Sawa, Resistive switching in transition metal oxides, Materials Today 11 (2008) 28–36.

[3] J. B. Goodenough, K.-S. Park, The li-ion rechargeable battery: A perspective, Journal of the American Chemical Society 135 (2013) 1167–1176. PMID: 23294028.

[4] J. Buckeridge, C. R. A. Catlow, M. R. Farrow, A. J. Logsdail, D. O. Scanlon, T. W. Keal, P. Sherwood, S. M. Woodley, A. A. Sokol, A. Walsh, Deep vs shallow nature of oxygen vacancies and consequent *n*-type carrier concentrations in transparent conducting oxides, Phys. Rev. Materials 2 (2018) 054604.

[5] L. Dong, R. Jia, B. Xin, B. Peng, Y. Zhang, Effects of oxygen vacancies on the structural and optical properties of β-Ga_2O_3, Scientific Reports 7 (2017) 40160.

[6] H. Mizoguchi, T. Kamiya, S. Matsuishi, H. Hosono, A germanate transparent conductive oxide, Nat. Commun. 2 (2011) 470.

[7] X. Zhou, Q. Zhang, L. Gan, X. Li, H. Li, Y. Zhang, D. Golberg, T. Zhai, High—performance solar-blind deep ultraviolet photodetector based on individual single-crystalline zn2geo4 nanowire, Advanced Functional Materials 26 (2016) 704–712.

[8] J. Huang, X. Wang, Y. Hou, X. Chen, L. Wu, X. Fu, Degradation of benzene over a zinc germanate photocatalyst under ambient conditions, Environmental Science & Technology 42 (2008) 7387–7391. PMID: 18939575.

[9] Z. Liu, X. Jing, L. Wang, Luminescence of native defects in Zn_2GeO_4, Journal of the Electrochemical Society 154 (2007) H500.

[10] J. Dolado, J. García-Fernández, P. Hidalgo, J. González-Calbet, J. Ramírez-Castellanos, B. Méndez, Intense cold-white emission due to native defects in Zn_2GeO_4 nanocrystals, Journal of Alloys and Compounds 898 (2022) 162993.

[11] Z. Cui, G. Deng, O. Wang, X. Luo, Z. Li, M. Yang, S. Cheng, X. Liu, Controllable synthesis and luminescence properties of Zn_2GeO_4:Mn^{2+} nanorod phosphors, ChemistrySelect 6 (2021) 10554–10560.

[12] T. T. Yu, H. Liu, M. Huang, J. H. Zhang, D. Q. Su, Z. H. Tang, J. F. Xie, Y. J. Liu, A. H. Yuan, Q. H. Kong, Zn_2GeO_4 nanorods grown on carbon cloth as high performance flexible lithium-ion battery anodes, RSC Adv. 7 (2017) 51807–51813.

[13] K. Punia, G. Lal, S. N. Dolia, S. Kumar, Defects and oxygen vacancies tailored structural, optical, photoluminescence and magnetic properties of Li doped ZnO nanohexagons, Ceramics International 46 (2020) 12296–12317.

[14] C. Rauch, W. Gehlhoff, M. R. Wagner, E. Malguth, G. Callsen, R. Kirste, B. Salameh, A. Hoffmann, S. Polarz, Y. Aksu, et al., Lithium related deep and shallow acceptors in Li-doped ZnO nanocrystals, Journal of Applied Physics 107 (2010) 024311.

[15] I. López, M. Alonso-Orts, E. Nogales, B. Méndez, J. Piqueras, Influence of Li doping on the morphology and luminescence of Ga_2O_3 microrods grown by a vapor-solid method, Semiconductor science and technology 31 (2016) 115003.

[16] R. Bhattacharjee, I.-M. Hung, Effect of different concentration Li-doping on the morphology, defect and photovoltaic performance of Li–ZnO nanofibers in the dye-sensitized solar cells, Materials Chemistry and Physics 143 (2014) 693–701.

[17] R. Dovesi, A. Erba, R. Orlando, C. Zicovich-Wilson, B. Civalleri, L. Maschio, M. Rerat, S. Casassa, J. Baima, S. Salustro, B. Kirtman, Quantum-mechanical condensed matter simulations with CRYSTAL, Wires Comput. Mol. Sci. 8 (2018) e1360.

[18] J. Heyd, S. GE, E. M, Hybrid functionals based on a screened coulomb potential, J. Chem. Phys. 118 (2003) 8207.

[19] J. Dolado, R. Martínez-Casado, P. Hidalgo, R. Gutierrez, A. Dianat, G. Cuniberti, F. Domínguez-Adame, E. Díaz, B. Méndez, Understanding the UV luminescence of zinc germanate: The role of native defects, Acta materialia 196 (2020) 626–634.

[20] M. Alonso-Orts, A. M. Sánchez, S. A. Hindmarsh, I. López, E. Nogales, J. Piqueras, B. Méndez, Shape engineering driven by selective growth of SnO_2 on doped Ga_2O_3 nanowires, Nano Letters 17 (2017) 515–522.

[21] M. García-Tecedor, D. Maestre, A. Cremades, J. Piqueras, Influence of Cr doping on the morphology and luminescence of SnO_2 nanostructures, The Journal of Physical Chemistry C 120 (2016) 22028–22034.

[22] Z. Song, J. Zhang, Y. Wang, J. Li, Influence of Li doping on the morphological evolution and optical & electrical properties of SnO_2 nanomaterials and SnO_2/Li_2SnO_3 composite nanomaterials, Ceramics International (2021).

[23] Y. Zhao, S. Yang, J. Zhu, G. Ji, F. Peng, The study of oxygen ion motion in Zn_2GeO_4 by raman spectroscopy, Solid State Ionics 274 (2015) 12–16.

[24] J. I. Viegas, R. L. Moreira, A. Dias, Optical-vibration properties of Li_2ZnGeO_4 dielectric ceramics, Vibrational Spectroscopy 110 (2020) 103130.

[25] V. Y. Suzuki, L. H. Amorin, G. S. Fabris, S. Dey, J. R. Sambrano, H. Cohen, D. Oron, F. A. La Porta, Enhanced photocatalytic and photoluminescence properties resulting from type-i band alignment in the Zn_2GeO_4/g-C_3N_4 nanocomposites, Catalysts 12 (2022) 692.

[26] Z.-Y. Xie, H.-L. Lu, Y. Zhang, Q.-Q. Sun, P. Zhou, S.-J. Ding, D. W. Zhang, The electronic structures and optical properties of Zn_2GeO_4 with native defects, Journal of Alloys and Compounds 619 (2015) 368–371.

[27] A. Molle, M. N. K. Bhuiyan, G. Tallarida, M. Fanciulli, In situ chemical and structural investigations of the oxidation of Ge (001) substrates by atomic oxygen, Applied physics letters 89 (2006) 083504.

[28] Y. Wang, S. R. Kavanagh, I. Burgués-Ceballos, A. Walsh, D. O. Scanlon, G. Konstantatos, Cation disorder engineering yields $AgBiS_2$ nanocrystals with enhanced optical absorption for efficient ultrathin solar cells, Nature Photonics 16 (2022) 235–241.

[29] S. Jana, S. Mukherjee, A. Ghorai, S. B. Bhaktha, S. K. Ray, Negative thermal quenching and size-dependent optical characteristics of highly luminescent phosphorene nanocrystals, Advanced Optical Materials 8 (2020) 2000180.

[30] M. A. Reshchikov, Mechanisms of thermal quenching of defect-related luminescence in semiconductors, physica status solidi (a) 218 (2021) 2000101.

[31] H.-S. Kwack, Y. Sun, Y.-H. Cho, N.-M. Park, S.-J. Park, Anomalous temperature dependence of optical emission in visible-light-emitting amorphous silicon quantum dots, Applied physics letters 83 (2003) 2901–2903.

[32] M. Watanabe, M. Sakai, H. Shibata, C. Satou, S. Satou, T. Shibayama, H. Tampo, A. Yamada, K. Matsubara, K. Sakurai, et al., Negative thermal quenching of photoluminescence in ZnO, Physica B: Condensed Matter 376 (2006) 711–714.

[33] Y. Wu, J. Li, H. Ding, Z. Gao, Y. Wu, N. Pan, X. Wang, Negative thermal quenching of photoluminescence in annealed ZnO–Al_2O_3 core–shell nanorods, Physical Chemistry Chemical Physics 17 (2015) 5360–5365.

[34] M. A. Reshchikov, Temperature dependence of defect-related photoluminescence in III−V and II−VI semiconductors, Journal of Applied Physics 115 (2014) 012010.

[35] K. Prashanthi, Ž. Antić, G. Thakur, M. D. Dramićanin, T. Thundat, Surface state-induced anomalous negative thermal quenching of multiferroic $BiFeO_3$ nanowires, physica status solidi (RRL) – Rapid Research Letters 12 (2018) 1700352.

[36] H. Shibata, Negative thermal quenching curves in photoluminescence of solids, Japanese Journal of Applied Physics 37 (1998) 550–553.

[37] J. Dolado, P. Hidalgo, B. Méndez, Kinetic study of the thermal quenching of the ultraviolet emission in Zn_2GeO_4 microrods, physica status solidi (RRL)–Rapid Research Letters (2022) 2100613.

[38] Y. Takahashi, M. Ando, K. Iwasaki, H. Masai, T. Fujiwara, Defect activation in willemite-type Zn_2GeO_4 by nanocrystallization, Applied Physics Letters 97 (2010) 071906.

[39] P. Hidalgo, J. Dolado, B. Méndez, Efficient white-light emission from Zn_2GeO_4 nanomaterials 10919 (2019) 218–224.

[40] L. Li, Y. Su, Y. Chen, M. Gao, Q. Chen, Y. Feng, Synthesis and photoluminescence properties of hierarchical zinc germanate nanostructures, Advanced Science Letters 3 (2010) 1–5.

[41] M. Wardle, J. Goss, P. Briddon, Theory of Li in ZnO: A limitation for Li-based p-type doping, Physical Review B 71 (2005) 155205.

[42] J. Yi, C. Lim, G. Xing, H. Fan, L. Van, S. Huang, K. Yang, X. Huang, X. Qin, B. Wang, et al., Ferromagnetism in dilute magnetic semiconductors through defect engineering: Li-doped ZnO, Physical review letters 104 (2010) 137201.

Supplementary Information

Li-doping effects on the native defects and luminescence of Zn$_2$GeO$_4$ microstructures: Negative thermal quenching

Jaime Dolado*[,a,b], Beatríz Rodríguez[a], Ruth Martínez-Casado[a], Igor Píš[c], Elena Magnano[c,d], Pedro Hidalgo[a] and Bianchi Méndez[a]

[a] *Departamento de Física de Materiales, Facultad de Ciencias Físicas, Universidad Complutense de Madrid, 28040-Madrid, Spain*

[b] *European Synchrotron Radiation Facility, 38043 Grenoble, France*

[c] *IOM-CNR, Istituto Officina dei Materiali, AREA Science Park Basovizza, 34149 Trieste, Italy*

[d] Department of Physics, University of Johannesburg, PO Box 524, Auckland Park, 2006 Johannesburg, South Africa
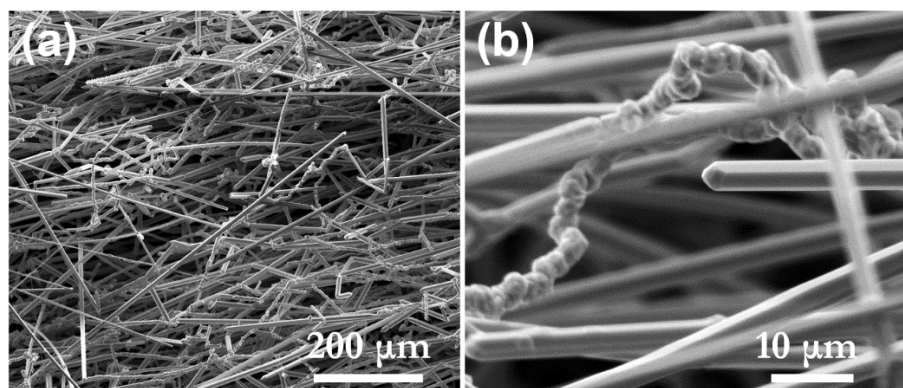
- Email: doladofe@esrf.fr

Supplementary Information

Figure SI-1 shows the comparison of the different samples grown with Li after thermal treatment, where it can be seen how the amount of structures obtained decreases with increasing Li concentration.
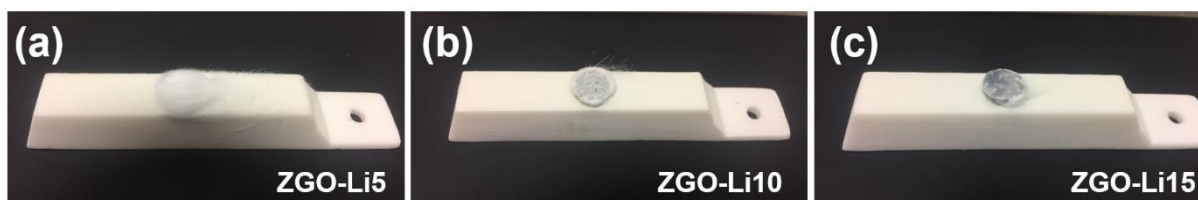

Figure SI-1. Photographs of (a) ZGO-Li5, (b) ZGO-Li10 and (c) ZGO-Li15 pellets after the thermal treatment.


Figure SI-2. (a) Low and (b) high magnification SE images of the mat of structures that have grown on the surface of the pellets, most of which are microrods.

|	Zn (At%)	Ge (At%)
Microrod	66.8 ± 1.5	33.2 ± 0.9
Distorted TLi5 structure	68.0 ± 2.2	32.0 ± 2.8
P-B TLi10 structure	64.8 ± 2.5	35.2 ± 3.5
Stratified TLi15 structure	49.7 ± 1.82	50.3 ± 4.5

Table SI-1. Atomic ratio Zn:Ge in individual structures obtained in each treatment, quantifying the intensity of the Zn *K-line* series and the Ge *L-line* series.
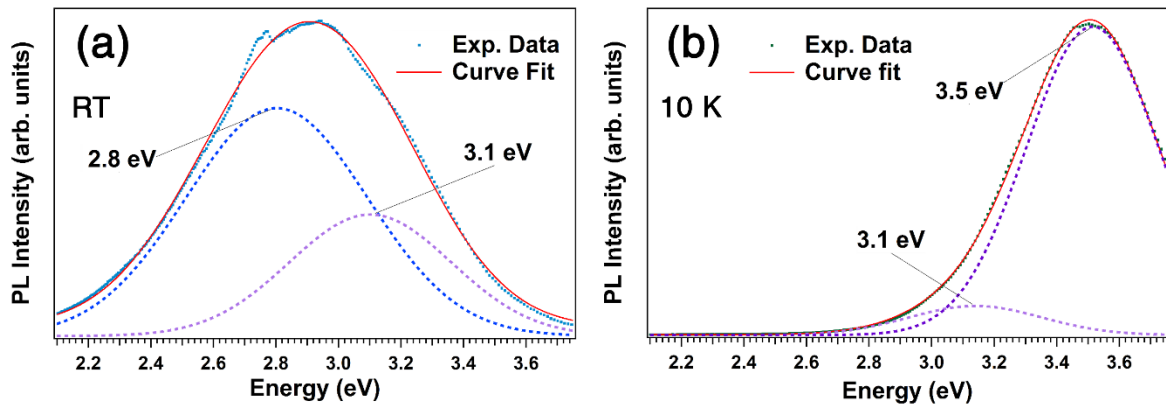
Figure SI-3. PL spectra of ZGO-Li10 sample collected at (a) RT and (b) 10 K with their respective Gaussian deconvolutions (dotted lines).
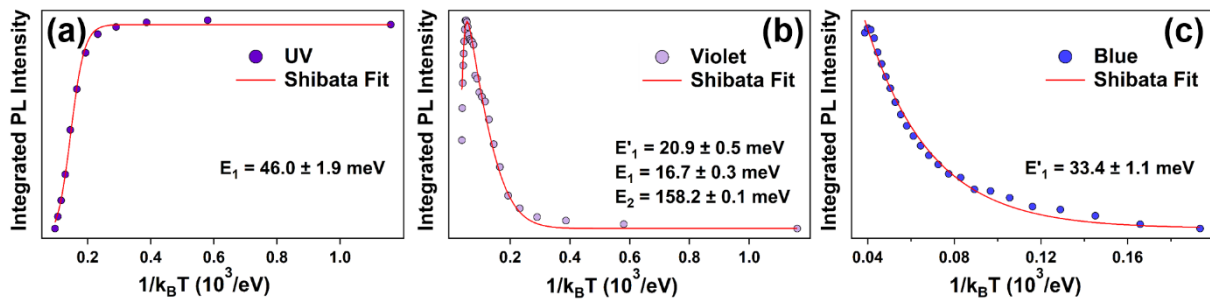
Figure SI-4. Integrated PL intensity of the (a) UV, (b) violet and (c) blue bands of ZGO-Li10 microrods as a function of $1/k_BT$. Experimental data (dots) are represented in comparison with a theoretical fitting (solid line) following the Shibata multi-level equation
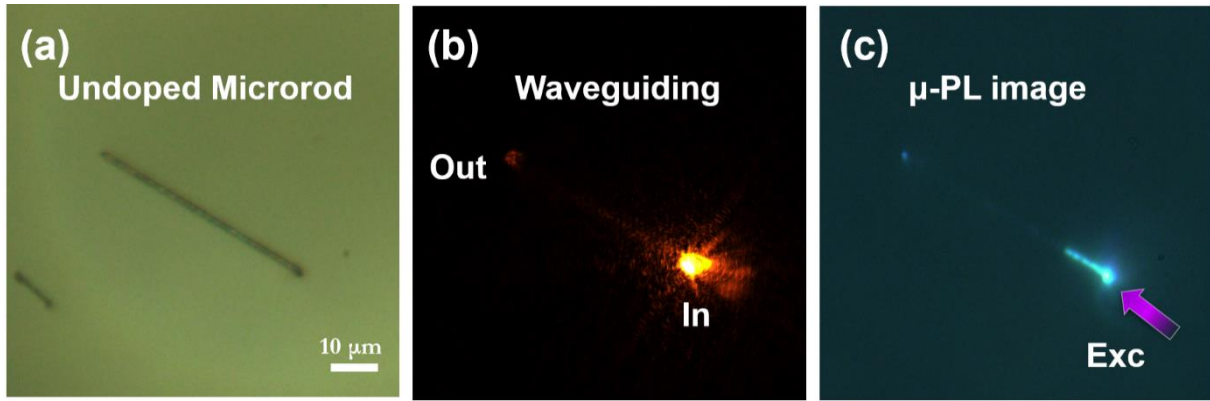
Figure SI-5. Optical images of a undoped ZGO microrod (a) without laser excitation and (b) under UV laser illumination in dark field showing the waveguiding behavior of the structure. (c) Dark field micro-PL image of the same microrod.

.

Element	Li_{Zn}	Li_i	$V_{Zn}\text{-}Li_{Zn}$	$V_{Zn}\text{-}Li_{Zn}\text{-}Li_i$
Ge	30.28	30.28	30.29	30.28
Zn	28.86	28.88	28.86	28.86
O	8.52	9.07	8.50	8.50
Li	2.29	2.23	2.29	2.29

Table SI-2. The Mulliken population (number of electrons) for the different atoms of the Li-doped ZGO.